

In situ synthesis of graphitic-C₃N₄ nanosheet hybridized N-doped TiO₂ nanofibers for efficient photocatalytic H₂ production and degradation

Cheng Han¹, Yingde Wang^{1,2} (✉), Yongpeng Lei^{3,4} (✉), Bing Wang¹, Nan Wu¹, Qi Shi¹, and Qiong Li²

¹ Science and Technology on Advanced Ceramic Fibers and Composites Laboratory, National University of Defense Technology, Changsha 410073, China

² College of Materials Science and Engineering, Wuhan Textile University, Wuhan 430074, China

³ College of Basic Education, National University of Defense Technology, Changsha 410073, China

⁴ State Key Laboratory of Low-Dimensional Quantum Physics and Department of Chemistry, Tsinghua University, Beijing 100084, China

Received: 29 July 2014

Revised: 26 September 2014

Accepted: 7 October 2014

© Tsinghua University Press
and Springer-Verlag Berlin
Heidelberg 2014

KEYWORDS

photocatalyst,
graphitic carbon nitride,
titanium oxide, nanofiber,
hydrogen production

ABSTRACT

Graphitic carbon nitride nanosheets (g-C₃N₄ NSs) hybridized nitrogen doped titanium dioxide (N-TiO₂) nanofibers (GCN/NT NFs) have been synthesized *in situ* via a simple electrospinning process combined with a modified heat-etching method. The prepared GCN/NT NFs were characterized by a variety of methods and their photocatalytic activities were evaluated by hydrogen (H₂) production from water splitting and degradation of rhodamine B in aqueous solution. It was found that the GCN/NT NFs have a mesoporous structure, composed of g-C₃N₄ NSs and N-doped TiO₂ crystallites. The g-C₃N₄ NSs synthesized after heat-etching were found to be embedded in, and covered, the hybrid NFs to form stable interfaces. The partial decomposition of g-C₃N₄ releases its nitrogen content which eventually gets doped into the nearby TiO₂ skeleton. The GCN/NT NFs give a high photocatalytic H₂ production rate of 8,931.3 μmol·h⁻¹·g⁻¹ in aqueous methanol solution under simulated solar light. Such a highly efficient photocatalytic performance can be ascribed to the combined effects of g-C₃N₄ NSs and N-doped TiO₂ with enhanced light absorption intensity and improved electron transport ability. Also, the large surface area of the mesoporous NFs minimizes light reflection on the surface and provides more surface-active sites. This work highlights the potential of quasi-one dimensional hybrid materials in the field of solar energy conversion.

1 Introduction

Photocatalysis technology, especially the photocatalytic

hydrogen (H₂) production from water splitting has been proven to be the most promising—but challenging—strategy for solving the global energy and environmental

Address correspondence to Yongpeng Lei, lypkd@163.com; Yingde Wang, wyd502@163.com

problems [1, 2]. Titanium dioxide (TiO_2) semiconductor has been widely used as a photocatalyst because of its environmental friendliness, low cost and long-term stability against photo and chemical corrosion [3–5]. Unfortunately, the high recombination ratio of photo-induced electron–hole pairs and the low solar energy conversion efficiency have hindered its application [6]. To solve these problems, considerable attempts have been devoted to designing and modifying TiO_2 , such as metal deposition [7–9], non-metal element doping [10] and surface sensitization [11, 12].

Among all these strategies mentioned above, coupling TiO_2 with other visible-light-responsive semiconductors to form heterojunction structures seems particularly meaningful and efficient [13, 14]. Graphitic carbon nitride ($\text{g-C}_3\text{N}_4$), for instance, with a band gap of ca. 2.7 eV and more negative conduction band than that of TiO_2 [15], has been utilized as a coupled semiconductor [16]. Recently, Yu et al. obtained a $\text{g-C}_3\text{N}_4$ – TiO_2 photocatalyst by a facile calcination route [17]. The space separation efficiency of photogenerated carriers was enhanced through a Z-scheme route. Also, Kubacka et al. reported the preparation of $\text{g-C}_3\text{N}_4$ loaded TiO_2 nanoparticles (NPs) using an impregnation method [18], and improved photocatalytic degradation activity of toluene was observed as a result of the efficient electron transfer at the heterojunction interface. However, since the $\text{g-C}_3\text{N}_4$ is just physically absorbed on the surface of TiO_2 NPs, the TiO_2 matrix must be activated under UV light irradiation, resulting in a limited utilization efficiency of solar light. Taking into account that nitrogen doping is also a very effective method to enhance the utilization efficiency of solar light for TiO_2 [10, 19], it would be a great advantage if a $\text{g-C}_3\text{N}_4$ hybridized N-doped TiO_2 photocatalyst could be designed and fabricated.

For most reported $\text{g-C}_3\text{N}_4$ based photocatalysts including $\text{g-C}_3\text{N}_4/\text{TiO}_2$ heterostructure [20–22], the preparation often involves calcination of mixtures containing organic precursors (such as cyanamide (urea)), resulting in composite NPs, which are prone to aggregation [23]. Additionally, the unpredictable microstructure of the $\text{g-C}_3\text{N}_4$ component inevitably restricts the practical application of these materials in photocatalysis. From the viewpoint of practical app-

lications and commercial benefits, the H_2 production activity of $\text{g-C}_3\text{N}_4$ based photocatalysts must be further enhanced. Recent theoretical and experimental investigations have revealed that, compared with bulk $\text{g-C}_3\text{N}_4$, $\text{g-C}_3\text{N}_4$ nanosheets (NSs) exhibit superior electronic and optical properties [15, 24–26]. For example, Liu et al. reported a graphene-like $\text{g-C}_3\text{N}_4$ NSs, obtained by a thermal oxidation etching treatment of bulk $\text{g-C}_3\text{N}_4$, which showed an attractive charge transport ability [26]. By a similar method, Wang et al. prepared $\text{g-C}_3\text{N}_4$ quantum dots from graphene-like $\text{g-C}_3\text{N}_4$ NSs, which exhibited the promise to be used as a general energy-transfer component in photocatalytic systems [27]. Therefore, it is expected that a graphene-like $\text{g-C}_3\text{N}_4$ NSs-based heterojunction will exhibit interesting properties which are beneficial for enhanced photocatalytic H_2 production activity.

In the present study, graphene-like $\text{g-C}_3\text{N}_4$ NSs hybridized N-doped TiO_2 nanofibers (GCN/NT NFs) with a stable interface and large surface area were synthesized by electrospinning combined with modified heat-etching (Fig. 1). The electrospinning technique is a low-cost, simple and continuous process for large-scale fabrication of continuous quasi-one dimensional (1D) fibers [28, 29]. Versatile 1D TiO_2 -based NFs have been patterned via the electrospinning, and shown to have distinct advantages in photocatalysis [30, 31]. Unlike composite NPs which have a loose granular form, the 1D NFs with large aspect ratio can provide a continuous transport pathway for the photogenerated charge carriers and are easily separated from solution [32–34]. In addition, graphene-like $\text{g-C}_3\text{N}_4$ NSs which were embedded in, and covered, the GCN/NT NFs were synthesized *in situ*. Moreover, during heat-etching, the partial decomposition of $\text{g-C}_3\text{N}_4$ releases its nitrogen content which eventually gets doped into the nearby TiO_2 skeleton [26, 35], further enhancing the visible light absorption. Meanwhile, the undoped TiO_2 part in the hybrid NFs can also absorb the UV region of solar light. We believe this is meaningful for the practical application of photocatalysts, since they can absorb and utilize different regions of the solar spectrum [36]. Our study provides a facile route for the *in situ* synthesis of quasi-1D heterojunction photocatalysts with great potential in the field of solar energy conversion.

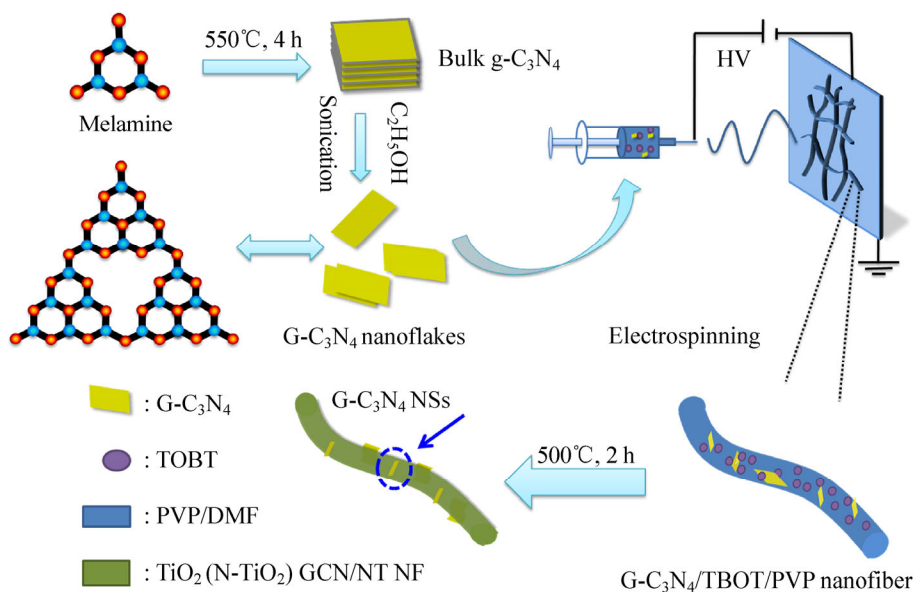


Figure 1 Schematic illustration of the fabrication of GCN/NT NFs.

2 Experimental

2.1 Materials

Poly(vinylpyrrolidone) (PVP, K-90, $M_w = 1.3 \times 10^6$ g·mol⁻¹) was bought from Shanghai Dibo Chemical Co., Ltd. Titanium(IV) n-butoxide (TNBT) was purchased from Shanghai Chemical Reagent Factory of China. Melamine was bought from Tianjin Guangfu Fine Chemical Research Institute. *N,N*-dimethylformamide (DMF, 99%) and acetic acid were obtained from Shanghai Titanchem. Co., Ltd. All chemicals were of analytical grade and used as received.

2.2 Preparation of GCN/NT NFs

The typical experimental procedure for the fabrication of GCN/NT NFs is illustrated in Fig. 1. Firstly, the bulk g-C₃N₄ was prepared by directly heating the melamine in a semi-closed system [37]. Certain amounts of g-C₃N₄ were then dispersed in ethanol and sonicated for 2 h to exfoliate bulk g-C₃N₄ [26]. Thereafter, PVP (1.18 g, 11 wt.%) was completely dissolved in the above suspension, followed by the addition of acetic acid (3 mL) and TNBT (1.5 g). The mixture was stirred for 12 h to form a homogeneous solution. Prior to electrospinning, the precursor solution was sonicated for 10 min and further loaded into a 10 mL plastic syringe with a needle of 0.7 mm inner diameter. A

high voltage of 14 kV was applied between the stainless steel nozzle and metal collector with a distance of 20 cm. Thereafter, the as-spun nanofibers were treated at 500 °C in air for 2 h to realise the *in situ* delamination of layered g-C₃N₄, at a heating rate of 5 °C·min⁻¹. The PVP component was eliminated at the same time. The final NFs are denoted as GCN/NT-*x*, where *x* denotes the mass of added g-C₃N₄ (0–0.2 g). N-doped TiO₂ (N-TiO₂) NFs were also prepared by further elimination of g-C₃N₄ at 650 °C for comparison.

2.3 Characterization

The crystal phases were identified by X-ray diffraction (XRD, Bruker AXS D8 ADVANCE) with Cu K α ($\lambda = 1.5406$ Å) radiation at a scanning rate of $2\theta = 0.02^\circ$ per step. The crystallite sizes were evaluated by the Scherrer equation from the XRD patterns. X-ray photoelectron spectra (XPS) were recorded on a Thermo Scientific ESCALAB 250Xi machine with an Al K α source. The morphological features were analyzed by a Hitachi S-4800 field-emission scanning electron microscope (FE-SEM) and JEM-2100HR high-resolution transmission electron microscope (HR-TEM). UV–vis diffuse reflectance spectra (DRS) were obtained using a U-4100 Hitachi Scan UV–vis spectrophotometer. Fourier transform infrared spectra (FTIR) were recorded on a Nicolet Avatar 360 (USA)

instrument on samples pressed as KBr pellets. The Brunauer–Emmett–Teller (BET) surface areas (S_{BET}) of samples were evaluated from nitrogen adsorption data recorded using a Micromeritics ASAP 2020 nitrogen adsorption apparatus. The pore size distributions were determined using adsorption data by the Barrett–Joyner–Halenda (BJH) method, assuming a cylindrical pore model. Photoluminescence (PL) emission spectra were used to investigate the fate of photogenerated electrons and holes in the sample, and were recorded on an F-7000 fluorescence spectrometer (Hitachi). The excitation wavelength was 350 nm with the scanning speed of 600 nm·min⁻¹. The widths of both excitation slit and emission slit were 10 nm.

2.4 Photocatalytic H₂ production

The photocatalytic H₂ production experiments were performed in a 100 mL three-neck quartz flask. A 300 W xenon arc lamp (Changzhou Siyu Environmental Materials Co., Ltd.) was used as a solar light source to trigger the photocatalytic reaction and was positioned 20 cm away from the reactor. In a typical experiment, 20 mg of the prepared GCN/NT NFs was dispersed with constant stirring in a 50 mL mixed solution of methanol (10 mL) and water (40 mL). A certain amount of H₂PtCl₆·6H₂O aqueous solution was then added dropwise into the system to load Pt onto the surface of the photocatalyst via a photochemical reduction deposition method. Prior to irradiation, the system was bubbled with nitrogen for 30 min to remove any residual O₂. After that, 1.0 mL sample of the generated gas was collected intermittently and analyzed by gas chromatography (SP6890, Shangdong Lunan Ruihong Instrument Co., Ltd., TCD, Ar as a carrier gas and 5 Å molecular sieve column).

2.5 Photocatalytic degradation tests

The synthesized GCN/NT NFs were also used to photodegrade rhodamine B (RhB) dye in aqueous solution. 0.1 g of catalyst was added to 100 mL of RhB aqueous solution (10 ppm) with a constant stirring rate at room temperature. Prior to irradiation, the solution was stirred for 30 min in dark to establish an adsorption/desorption equilibrium. At scheduled irradiation time intervals, 3 mL of the suspension was

withdrawn and the dynamic RhB concentration was analyzed by a 722S visible spectrophotometer (INESA Scientific Instrument Co., Ltd.) at 554 nm.

3 Results and discussion

In order to investigate the effect of thermal treatment on the crystal structure of g-C₃N₄, comparative XRD patterns before and after further treatment at 500 °C are given in Fig. 2(a). For bulk g-C₃N₄, the strongest diffraction peak at $2\theta = 27.4^\circ$ corresponding to 0.326 nm is due to the stacking of the conjugated aromatic system, while the peak at about 13.0° corresponds to 0.680 nm, represents the in-plane structural packing

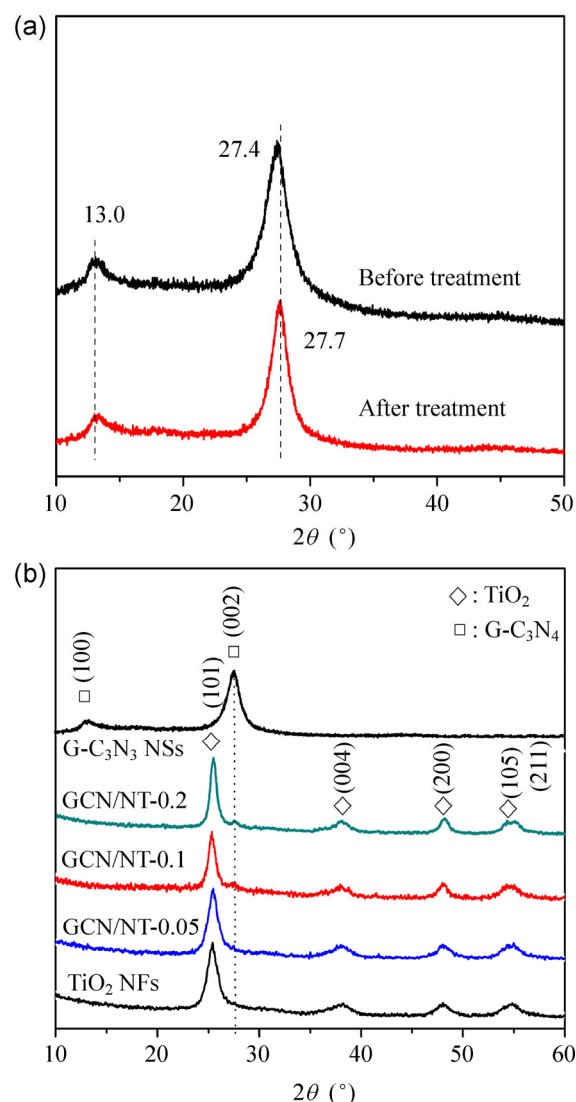


Figure 2 XRD patterns of (a) g-C₃N₄ before and after further treatment at 500 °C and (b) g-C₃N₄, TiO₂ and GCN/NT-*x* NFs.

motif [15]. After heat-etching, the sample gives two peaks consistent with the pattern for bulk $\text{g-C}_3\text{N}_4$, suggesting that the $\text{g-C}_3\text{N}_4$ retains its microstructure well. It is noteworthy that the strongest diffraction peak was shifted from 27.4° to 27.7° , indicating a slight decrease in interlayer distance. It is also observed that the low-angle reflection peak at 13.0° became less pronounced after heat treatment. These results are in good agreement with previous reports [24–26], indicating the successful production of graphene-like $\text{g-C}_3\text{N}_4$ NSs after further treatment at 500°C . Figure 2(b) shows the XRD patterns of GCN/NT- x samples. The characteristic diffraction peaks of TiO_2 can be ascribed to anatase (JCPDS, No. 21-1272). The intensity of the diffraction peak at 27.6° increases slightly after the introduction of $\text{g-C}_3\text{N}_4$. The hybrid NFs are composed of small TiO_2 crystallites having sizes of approximately 10 nm, evaluated by the Scherrer equation from the XRD patterns.

The hybridized $\text{g-C}_3\text{N}_4$ NSs on the surface of the GCN/NT NFs can be directly observed in the TEM images in Fig. 3. As seen in Fig. 3(a), the bulk $\text{g-C}_3\text{N}_4$ was exfoliated to give nanoflakes after sonication. The hybrid NFs are relatively uniform with a diameter of ~ 100 nm (Fig. 3(b)). Also, as revealed by the electron diffraction rings (inset in Fig. 3(c)), the electrospun NFs are composed of nanoscale TiO_2 crystallites, in good agreement with the above XRD analysis. Intimately stacked TiO_2 crystallites in GCN/NT NFs can minimize light reflection on the surface and impressively enhance the electron diffusion coefficient [32, 38]. The lattice spacing is measured to be 0.35 nm (Fig. 3(d)), corresponding to the prominent (101) plane of anatase TiO_2 [39]. On the basis of above XRD analysis, the hydrogen bonds between the layers of $\text{g-C}_3\text{N}_4$ could be gradually destroyed after heat-etching at 500°C , and thus graphene-like $\text{g-C}_3\text{N}_4$ NSs were synthesized *in situ* [25, 27] and were embedded in, and covered, the hybrid NFs (shown by arrows in Figs. 3(c) and 3(d)). The graphene-like structure of $\text{g-C}_3\text{N}_4$ was also observed in the TEM image of the GCN/NT-0.2 sample (Fig. S1 in the Electronic Supplementary Material, (ESM)). Such a stable interface between $\text{g-C}_3\text{N}_4$ and TiO_2 should contribute to the improved transfer of charge carriers.

FTIR is a useful tool to prove the presence of $\text{g-C}_3\text{N}_4$

in the hybrid NFs. Figure 4 illustrates the FTIR spectra of pure $\text{g-C}_3\text{N}_4$ and GCN/NT NFs. For pristine $\text{g-C}_3\text{N}_4$, several strong bands are observed in the region $1,200$ – $1,650\text{ cm}^{-1}$, with peaks at about $1,639$, $1,571$, $1,459$, $1,410$, $1,327$ and $1,250\text{ cm}^{-1}$, which can be ascribed to the typical stretching modes of CN heterocycles [17]. Additionally, the broad band at around $3,200\text{ cm}^{-1}$ is assigned to N–H and O–H stretching vibration modes, while the sharp peak at about 805 cm^{-1} is due to the characteristic breathing mode of tri-s-triazine units [22]. For GCN/NT NFs, the main peaks appearing at 400 – 700 cm^{-1} are attributed to Ti–O stretching and Ti–O–Ti bridging stretching

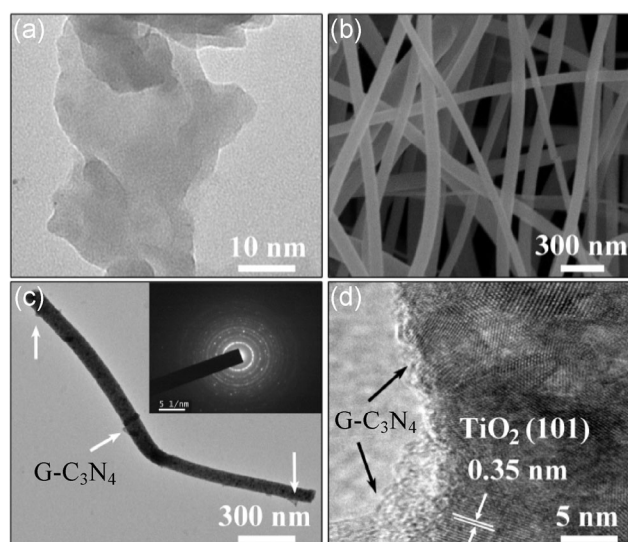


Figure 3 (a) TEM image of $\text{g-C}_3\text{N}_4$ nanoflakes, (b) SEM image of GCN/NT-0.1, (c) TEM image of a single GCN/NT-0.1 NF and (d) HRTEM image of GCN/NT-0.1 NF. Inset in (c) is the corresponding selected-area electron diffraction rings.

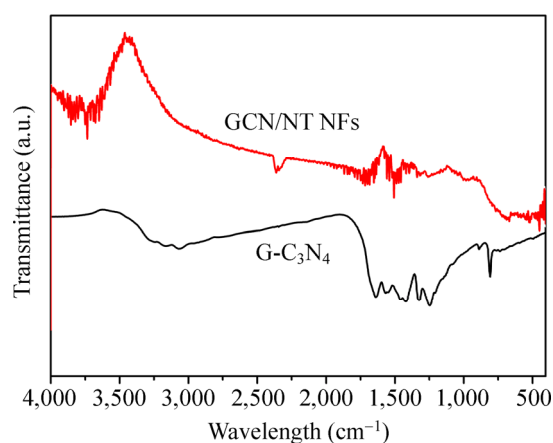


Figure 4 FTIR spectra of pure $\text{g-C}_3\text{N}_4$ and GCN/NT NFs (using the sample GCN/NT-0.1).

modes in TiO_2 . Also, the broad absorption bands at around 1,200–1,650 and 805 cm^{-1} are attributed to the characteristic stretching modes of $\text{g-C}_3\text{N}_4$, suggesting the presence of $\text{g-C}_3\text{N}_4$ in the hybrid NFs.

To further evaluate the chemical composition as well as chemical state of the elements in the prepared samples, XPS was performed. Figure 5 shows the XPS survey spectrum and high-resolution XPS of C, N and Ti elements in GCN/NT-0.1 sample. As seen in Fig. 5(a), the GCN/NT NFs are composed of Ti, O, C and N elements. The high-resolution XPS of C 1s provided in Fig. 5(b) can be deconvoluted into two peaks, which are ascribed to the adventitious carbon at 284.6 eV and the carbon atom in the N-C=N group at 288.1 eV [40]. The N 1s spectrum in Fig. 5(c) can be fitted with four peaks. The peaks centered at 398.6 and 400.6 eV are attributed to the sp^2 -hybridized nitrogen (C=N-C) involved in the triazine rings and the quaternary nitrogen bonded to three carbon atoms in the aromatic rings [41], respectively. The peak at about 404.2 eV is derived from charging effects or

positive charge localization in heterocycles [40]. Although the peak at about 399.5 eV may be ascribed to the tertiary nitrogen in the form of N-C_3 or H-N-C_2 according to previous reports [42, 43], it is notable that there is no similar peak for pure $\text{g-C}_3\text{N}_4$ NFs. (Fig. S2, in the ESM). Taking into account that the binding energy of the incorporated nitrogen dopant in TiO_2 as interstitial N or O-Ti-N is also located at 399.5 eV [16], this suggests that nitrogen might have been doped into the TiO_2 lattice during heat-etching. We give the comparative Ti 2p spectra of pure TiO_2 NFs and GCN/NT NFs in Fig. 5(d). Interestingly, a slight shift in the binding energy of $\text{Ti } 2\text{p}_{3/2}$ is observed as compared to pure TiO_2 NFs, suggesting a change in the electron density distribution on the Ti atoms. The negative shift in the $\text{Ti } 2\text{p}_{3/2}$ binding energy from 458.8 to 458.5 eV can be ascribed to the presence of nitrogen species in the TiO_2 lattice [22], because of the lower electronegativity of N compared to O which leads to partial electron transfer from the N to the Ti [44]. We therefore draw the conclusion that

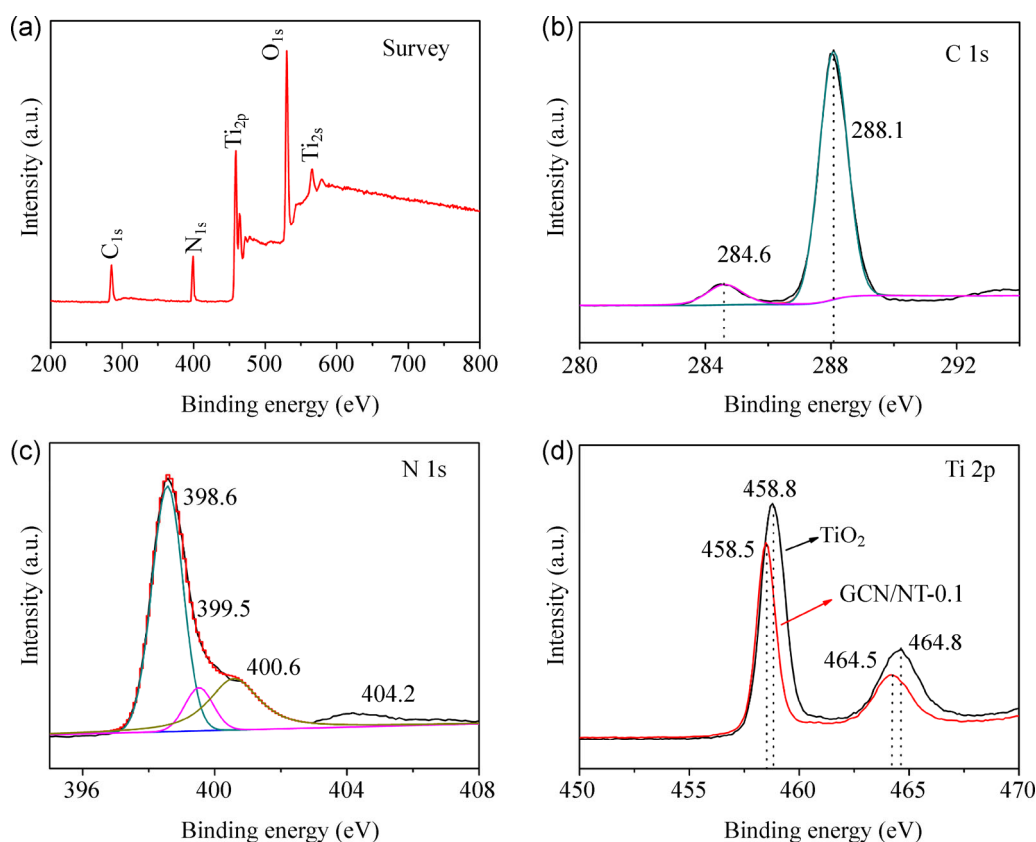


Figure 5 (a) XPS survey spectrum and the high resolution XPS of (b) C 1s, (c) N 1s of GCN/NT-0.1 NFs and (d) Ti 2p for the TiO_2 and GCN/NT-0.1 NFs.

nitrogen is successfully doped into TiO_2 lattice, aroused by the released nitrogen content from the partial decomposition of $\text{g-C}_3\text{N}_4$ [26, 35]. It is known that nitrogen doping is a very effective strategy to enhance the utilization efficiency of solar light [10], which plays an important role in increasing the photocatalytic activity of TiO_2 .

For a better understanding of the optical absorption performance of GCN/NT NFs, the UV-vis DRS were measured and the results are given in Fig. 6. The band gaps of $\text{g-C}_3\text{N}_4$ and TiO_2 are estimated to be about 2.7 and 3.2 eV, with the absorption edges at about 465 and 390 nm, respectively. All the GCN/NT- x samples exhibit absorbance in the visible light region, with the absorption edge intermediate between those of $\text{g-C}_3\text{N}_4$ and TiO_2 . Such red shifts might be a result of the intrinsic high visible light absorption of $\text{g-C}_3\text{N}_4$ and/or the nitrogen dopant in TiO_2 as mentioned above. It is worthy of note that, the N-doped TiO_2 and $\text{g-C}_3\text{N}_4$ display absorption in visible light region, while the undoped TiO_2 part in the GCN/NT NFs can strongly absorb UV light. Thus, the prepared GCN/NT NFs can efficiently absorb and utilize different regions of the solar spectrum, which is meaningful for the practical application of photocatalysts under solar light.

To have an insight into the effect of the embedded $\text{g-C}_3\text{N}_4$ NSs on the porous structure of GCN/NT NFs, BET analysis was carried out. The corresponding nitrogen adsorption/desorption isotherms of pure TiO_2 NFs, GCN/NT-0.05 and GCN/NT-0.1 are presented in Fig. 7. Both TiO_2 and GCN/NT NFs have isotherms of type IV according to the IUPAC classification [45], indicating the presence of mesopores (2–50 nm). Furthermore, the isotherm profiles show typical H_2 type hysteresis loops in the relative pressure range from 0.4 to 0.9 and hysteresis loops close to H_3 type from 0.9 to 1.0, indicating the presence of slit-like pores [46]. The pore size distribution of GCN/NT-0.1 NFs exhibits a broadened pore size range (inset in Fig. 7). The S_{BET} and average pore width of all the samples are given in Table S1 (in the ESM). The bulk $\text{g-C}_3\text{N}_4$ prepared by directly heating melamine has a low surface area of $4.1 \text{ m}^2\cdot\text{g}^{-1}$. After heat-etching treatment, the surface area of the resulting $\text{g-C}_3\text{N}_4$ NSs increased to $16.0 \text{ m}^2\cdot\text{g}^{-1}$. Both the GCN/NT-0.1 and GCN/NT-0.05 NFs have larger surface areas than

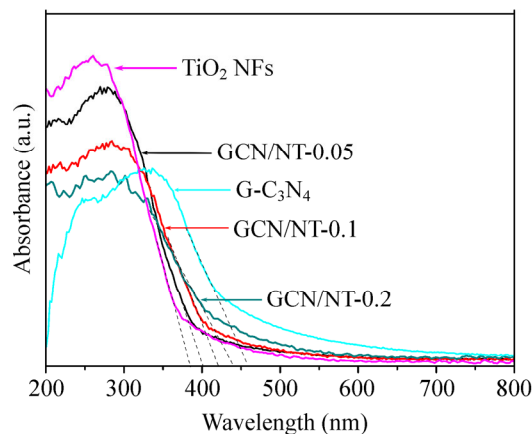


Figure 6 UV-vis DRS spectra of TiO_2 NFs, $\text{g-C}_3\text{N}_4$ and GCN/NT- x samples.

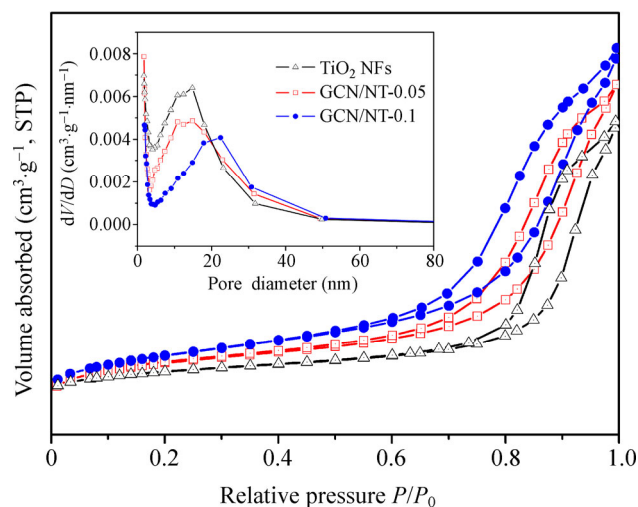


Figure 7 Nitrogen adsorption/desorption isotherms of TiO_2 , GCN/NT-0.05 and GCN/NT-0.1 NFs. The inset shows the pore-size distributions.

pure TiO_2 NFs due to the embedded $\text{g-C}_3\text{N}_4$ NSs, and in particular the GCN/NT-0.1 NFs have a high surface area of $47.3 \text{ m}^2\cdot\text{g}^{-1}$. Thus, the presence of the hybridized $\text{g-C}_3\text{N}_4$ NSs in the GCN/NT NFs greatly increases the specific surface areas and broadens the range of mesopores, which should be beneficial in terms of providing more surface-active sites for photocatalysis processes.

Photocatalytic H_2 production experiments were performed using the samples of pristine $\text{g-C}_3\text{N}_4$, TiO_2 , N- TiO_2 and GCN/NT-0.1 NFs. As shown in Fig. 8, the GCN/NT-0.1 NFs exhibit the highest H_2 production activity in aqueous methanol solution, with a rate of $8,931.3 \mu\text{mol}\cdot\text{h}^{-1}\cdot\text{g}^{-1}$. After further treatment at 650°C , the H_2 evolution rate decreases to $7,557.9 \mu\text{mol}\cdot\text{h}^{-1}\cdot\text{g}^{-1}$

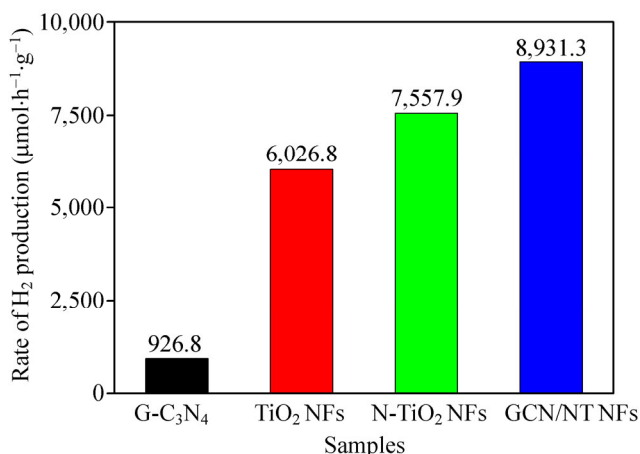


Figure 8 Photocatalytic H₂ production rate for TiO₂ NFs, g-C₃N₄ and GCN/NT NFs (using the sample GCN/NT-0.1) in aqueous methanol solution under simulated solar light.

(the N-TiO₂ sample), demonstrating that the g-C₃N₄ plays a key role in the high activity of the GCN/NT NFs. The stability of GCN/NT NFs was evaluated by performing catalyst recycling experiments under similar conditions (Fig. S3, in the ESM). After three cycles, H₂ production did not change significantly, indicating sufficient durability of such GCN/NT NFs for H₂ generation. SEM images of the hybrid NFs before and after three H₂ production cycles are given in Fig. S4 (in the ESM). The sample still retains the original shape of the NFs, demonstrating that the NFs can efficiently suppress the aggregation of nano-scale TiO₂ crystallites.

The photocatalytic activity of GCN/NT NFs was also evaluated using the degradation of RhB dye in aqueous solution as a probe reaction. As shown in Fig. 9, the photolysis of RhB in the absence of a catalyst is negligible. The TiO₂ NFs show weak catalytic activity, with only ~40% of RhB being degraded after irradiation for 150 min. There are two main reasons that contribute to such low photocatalytic activity. One is that TiO₂ absorbs a lower proportion of UV light in simulated solar light. The other one is the high recombination ratio of photoinduced electron-hole pairs. The g-C₃N₄ NSs obtained by thermal treatment of bulk g-C₃N₄, have a higher activity than TiO₂ NFs and bulk g-C₃N₄. The GCN/NT-0.1 NFs exhibit the highest activity, with the RhB being completely degraded in 120 min (inset in Fig. 9). The photocatalytic degradation was found to be a pseudo-first-order

kinetic process, which can be expressed by the equation

$$-\ln(C/C_0) = kt$$

where k is the pseudo-first-order rate constant, and C_0 and C are concentrations of RhB at times 0 and t , respectively. The GCN/NT-0.1 NFs exhibits the highest first-order rate constant of 0.0321 min⁻¹, which is 7.3 times higher than that of TiO₂ NFs (0.0044 min⁻¹) and 3.6 times higher than that of g-C₃N₄ (0.0089 min⁻¹).

On the basis of the above results, a synergistic mechanism, involving N-TiO₂ NPs and g-C₃N₄ NSs in the GCN/NT NFs, can be invoked to explain the enhanced photocatalytic H₂ production activity (Fig. 10). The conduction band (CB) and valence band (VB)

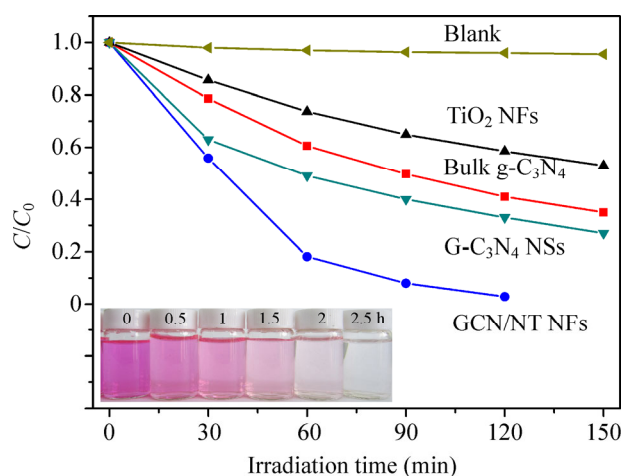


Figure 9 The percentage photodegradation of RhB for the samples TiO₂ NFs, bulk g-C₃N₄, g-C₃N₄ NSs and GCN/NT NFs (using the sample GCN/NT-0.1) under simulated solar light. The inset shows the variation with time of the color of the RhB solution for GCN/NT NFs as a photocatalyst.

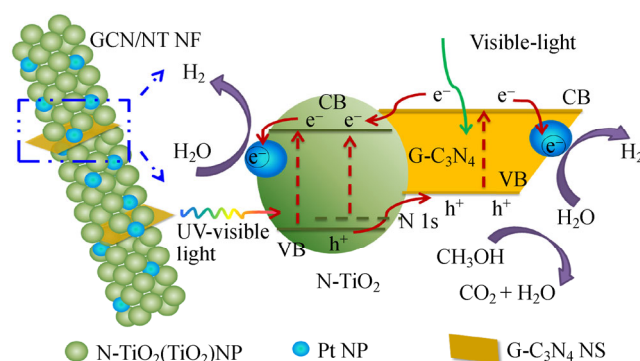


Figure 10 Proposed synergistic mechanism involving N-TiO₂ and g-C₃N₄ in the GCN/NT NFs for the enhanced photocatalytic H₂ production activity.

potentials of $g\text{-C}_3\text{N}_4$ are estimated to be -1.12 and $+1.57$ eV [15], and the CB and VB of TiO_2 are at -0.29 and $+2.91$ eV [17], respectively. The N-doped TiO_2 can efficiently enhance the visible light absorption. Meanwhile, the undoped TiO_2 part in the hybrid NFs can also absorb the UV light. Under UV-vis light irradiation, the photogenerated electrons of $g\text{-C}_3\text{N}_4$ readily transfer to the CB of TiO_2 , while the holes migrate from the VB of TiO_2 to the VB of $g\text{-C}_3\text{N}_4$. Thus the recombination of photogenerated electrons and holes is sufficiently inhibited, leaving more electrons in the CB of TiO_2 and more holes in the VB of $g\text{-C}_3\text{N}_4$. The transferred electrons accumulate on the Pt NPs loaded on the NFs and then participate in H_2 generation. In addition, the graphene-like structure of $g\text{-C}_3\text{N}_4$ contributes significantly to the improved electron transport. Also, the large surface area of the mesoporous NFs minimizes light reflection on the surface and provides more surface-active sites.

To test the above explanation, PL studies were performed since they reveal the efficiency of charge carrier trapping, transfer, and separation. As shown in Fig. 11, pure $g\text{-C}_3\text{N}_4$ exhibits strong photoluminescence with an emission peak at about 460 nm, which is in accordance with UV-vis DRS analysis. The PL spectrum of TiO_2 NFs in the wavelength range 380–450 nm is ascribed to a band–band PL emission phenomenon and excitonic PL resulting from surface oxygen vacancies and defects [47]. The broad but weaker PL spectrum of GCN/NTNFs reflects the

combined effect of both the $g\text{-C}_3\text{N}_4$ and TiO_2 (N- TiO_2) components, indicating a lower recombination rate of photoinduced electrons and holes.

4 Conclusion

We have developed a facile route for *in situ* synthesis of a continuous quasi-1D heterojunction photocatalyst with large surface area. The mesoporous GCN/NT NFs prepared using this method are composed of graphene-like $g\text{-C}_3\text{N}_4$ NSs and nanoscale N-doped TiO_2 crystallites, which are both important in enhancing the light absorption intensity and ability to transport charges. The GCN/NT NFs present highly efficient photocatalytic H_2 production and degradation activity under simulated solar light, due to the synergistic effect between the $g\text{-C}_3\text{N}_4$ NSs and N-doped TiO_2 . We hope this work will pave the way to further improve the solar energy conversion efficiency of TiO_2 -based photocatalysts.

Acknowledgements

The work was financially supported by the National Natural Science Foundation of China (Nos. 51173202 and 51203182), Hunan Provincial Natural Science Foundation (No. 13JJ4009), Open Research Fund Program of the State Key Laboratory of Low-Dimensional Quantum Physics (No. KF201312), State Key Laboratory of Advanced Technology for Materials Synthesis and Processing (Wuhan University of Technology) (No. 2014-KF-10), State Key Laboratory for Mechanical Behavior of Materials, Xi'an Jiaotong University (No. 20131304), Guangxi Key Laboratory of Information Materials (Guilin University of Electronic Technology) (No. 1210908-01-K), State Key Laboratory for Modification of Chemical Fibers and Polymer Materials, Dong Hua University (No. LK1207), Key Laboratory of Advanced Textile Materials and Manufacturing Technology (Zhejiang Sci-Tech University), Ministry of Education (No. 2013002), Aid Program for Science and Technology Innovative Research Team in Higher Educational Institutions of Hunan Province and Aid Program for Innovative Group of National University of Defense Technology.

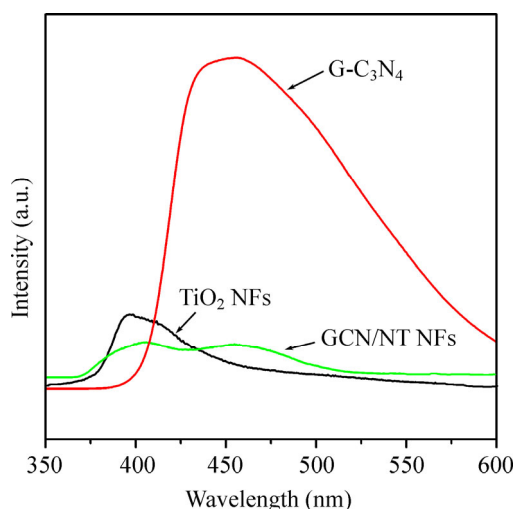


Figure 11 PL spectra of TiO_2 NFs, $g\text{-C}_3\text{N}_4$ and GCN/NT NFs (using the sample GCN/NT-0.1).

Electronic Supplementary Material: Supplementary material (further TEM images, N 1s XPS, photocatalytic durability measurements and SBET results of studied samples) is available in the online version of this article at <http://dx.doi.org/10.1007/s12274-014-0600-2>.

References

- [1] Wang, H. L.; Zhang, L. S.; Chen, Z. G.; Hu, J. Q.; Li, S. J.; Wang, Z. H.; Liu, J. S.; Wang, X. C. Semiconductor heterojunction photocatalysts: Design, construction, and photocatalytic performances. *Chem. Soc. Rev.* **2014**, *43*, 5234–5244.
- [2] Cao, S. W.; Yu, J. G. G-C₃N₄-based photocatalysts for hydrogen generation. *J. Phys. Chem. Lett.* **2014**, *5*, 2101–2107.
- [3] Fujishima, A.; Honda, K. Electrochemical photolysis of water at a semiconductor electrode. *Nature* **1972**, *238*, 37–38.
- [4] Xiang, Q. J.; Yu, J. G.; Jaroniec, M. Synergetic effect of MoS₂ and graphene as cocatalysts for enhanced photocatalytic H₂ production activity of TiO₂ nanoparticles. *J. Am. Chem. Soc.* **2012**, *134*, 6575–6578.
- [5] Ong, W. J.; Tan, L. L.; Chai, S. P.; Yong, S. T.; Mohamed, A. R. Self-assembly of nitrogen-doped TiO₂ with exposed {001} facets on a graphene scaffold as photo-active hybrid nanostructures for reduction of carbon dioxide to methane. *Nano Res.* **2014**, *7*, 1528–1547.
- [6] Wu, N.; Wang, Y. D.; Lei, Y. P.; Wang, B. Preparation and photocatalytic activity of N-Ag co-doped TiO₂/C porous ultrafine fibers mat. *Ceram. Int.* **2014**, *40*, 2017–2022.
- [7] Nguyen, N. T.; Yoo, J. E.; Altomare, M.; Schmuki, P. “Suspended” Pt nanoparticles over TiO₂ nanotubes for enhanced photocatalytic H₂ evolution. *Chem. Commun.* **2014**, *50*, 9653–9656.
- [8] Zhou, W.; Li, T.; Wang, J. Q.; Qu, Y.; Pan, K.; Xie, Y.; Tian, G. H.; Wang, L.; Ren, Z. Y.; Jiang, B. J. et al. Composites of small Ag clusters confined in the channels of well-ordered mesoporous anatase TiO₂ and their excellent solar-light-driven photocatalytic performance. *Nano Res.* **2014**, *7*, 731–742.
- [9] Wang, P.; Han, L.; Zhu, C. Z.; Zhai, Y. M.; Dong, S. J. Aqueous-phase synthesis of Ag-TiO₂-reduced graphene oxide and Pt-TiO₂-reduced graphene oxide hybrid nanostructures and their catalytic properties. *Nano Res.* **2011**, *4*, 1153–1162.
- [10] Asahi, R.; Morikawa, T.; Ohwaki, T.; Aoki, K.; Taga, Y. Visible-light photocatalysis in nitrogen-doped titanium oxides. *Science* **2001**, *293*, 269–271.
- [11] Zhang, H. J.; Xu, P. P.; Du, G. D.; Chen, Z. W.; Oh, K.; Pan, D. Y.; Jiao, Z. A facile one-step synthesis of TiO₂/graphene composites for photodegradation of methyl orange. *Nano Res.* **2011**, *4*, 274–283.
- [12] Shen, J. F.; Shi, M.; Ma, H. W.; Li, N.; Ye, M. X. Ionic liquid-assisted one-step hydrothermal synthesis of TiO₂-reduced graphene oxide composites. *Nano Res.* **2011**, *4*, 795–806.
- [13] Chen, C. C.; Ma, W. H.; Zhao, J. C. Semiconductor-mediated photodegradation of pollutants under visible-light irradiation. *Chem. Soc. Rev.* **2010**, *39*, 4206–4219.
- [14] Shi, J. L. On the synergetic catalytic effect in heterogeneous nanocomposite catalysts. *Chem. Rev.* **2013**, *113*, 2139–2181.
- [15] Wang, X. C.; Maeda, K.; Thomas, A.; Takanabe, K.; Xin, G.; Carlsson, J. M.; Domen, K.; Antonietti, M. A metal-free polymeric photocatalyst for hydrogen production from water under visible light. *Nat. Mater.* **2009**, *8*, 76–80.
- [16] Chai, B.; Peng, T. Y.; Mao, J.; Li, K.; Zan, L. Graphitic carbon nitride (g-C₃N₄)-Pt-TiO₂ nanocomposite as an efficient photocatalyst for hydrogen production under visible light irradiation. *Phys. Chem. Chem. Phys.* **2012**, *14*, 16745–16752.
- [17] Yu, J. G.; Wang, S. H.; Low, J. X.; Xiao, W. Enhanced photocatalytic performance of direct Z-scheme g-C₃N₄/TiO₂ photocatalyst for decomposition of formaldehyde in air. *Phys. Chem. Chem. Phys.* **2013**, *15*, 16883–16890.
- [18] Muñoz-Batista, M. J.; Kubacka, A.; Fernández-García, G. Effect of g-C₃N₄ loading in TiO₂-based photocatalysts: UV and visible degradation of toluene. *Catal. Sci. Technol.* **2014**, *4*, 2006–2015.
- [19] Liu, G.; Yang, H. G.; Wang, X.; Cheng, L.; Pan, J.; Lu, G. Q.; Cheng, H. M. Visible light responsive nitrogen doped anatase TiO₂ sheets with dominant {001} facets derived from TiN. *J. Am. Chem. Soc.* **2009**, *131*, 12868–12869.
- [20] Wang, Y. J.; Shi, R.; Lin, J.; Zhu, Y. F. Enhancement of photocurrent and photocatalytic activity of ZnO hybridized with graphite-like C₃N₄. *Energy Environ. Sci.* **2011**, *4*, 2922–2929.
- [21] Huang, L. Y.; Xu, H.; Li, Y. P.; Li, H. M.; Cheng, X. N.; Xia, J. X.; Xu, Y. G.; Cai, G. B. Visible-light-induced WO₃/g-C₃N₄ composites with enhanced photocatalytic activity. *Dalton Trans.* **2013**, *42*, 8606–8616.
- [22] Zhou, S.; Liu, Y.; Li, J. M.; Wang, Y. J.; Jiang, G. Y.; Zhao, Z.; Wang, D. X.; Duan, A. H.; Liu, J.; Wei, Y. C. Facile *in situ* synthesis of graphitic carbon nitride (g-C₃N₄)-N-TiO₂ heterojunction as an efficient photocatalyst for the selective photoreduction of CO₂ to CO. *Appl. Catal. B-Environ.* **2014**, *158*, 20–29.
- [23] Kim, C. H.; Kim, B. H.; Yang, K. S. TiO₂ nanoparticles loaded on graphene/carbon composite nanofibers by electrospinning for increased photocatalysis. *Carbon* **2012**, *50*, 2472–2481.

- [24] Wang, W. J.; Yu, J. C.; Xia, D. H.; Wong, P. K.; Li, Y. C. Graphene and g-C₃N₄ nanosheets cowrapped elemental α -sulfur as a novel metal-free heterojunction photocatalyst for bacterial inactivation under visible-light. *Environ. Sci. Technol.* **2013**, *47*, 8724–8732.
- [25] Yang, S. B.; Gong, Y. J.; Zhang, J. S.; Zhan, L.; Ma, L. L.; Fang, Z. Y.; Vajtai, R.; Wang, X. C.; Jayan, P. M. Exfoliated graphitic carbon nitride nanosheets as efficient catalysts for hydrogen evolution under visible light. *Adv. Mater.* **2013**, *25*, 2452–2456.
- [26] Niu, P.; Zhang, L. L.; Liu, G.; Cheng, H. M. Graphene-like carbon nitride nanosheets for improved photocatalytic activities. *Adv. Funct. Mater.* **2012**, *22*, 4763–4770.
- [27] Wang, W. J.; Yu, J. C.; Shen, Z. R.; Chan, D. K. L.; Gu, T. g-C₃N₄ quantum dots: Direct synthesis, upconversion property and photocatalytic application. *Chem. Commun.* **2014**, *50*, 10148–10150.
- [28] Wang, Y. D.; Han, C.; Zheng, D. C.; Lei, Y. P. Large-scale, flexible and high-temperature resistant ZrO₂/SiC ultrafine fibers with a radial gradient composition. *J. Mater. Chem. A* **2014**, *2*, 9607–9612.
- [29] Zhang, C. L.; Yu, S. H. Nanoparticles meet electrospinning: Recent advances and future prospects. *Chem. Soc. Rev.* **2014**, *43*, 4423–4448.
- [30] Fu, J. W.; Cao, S. W.; Yu, J. G.; Low, J. X.; Lei, Y. P. Enhanced photocatalytic CO₂-reduction activity of electrospun mesoporous TiO₂ nanofibers by solvothermal treatment. *Dalton Trans.* **2014**, *43*, 9158–9165.
- [31] Wu, N.; Wang, Y. D.; Lei, Y. P.; Wang, B.; Han, C. Flexible N-doped TiO₂/C ultrafine fiber mat and its photocatalytic activity under simulated sunlight. *Appl. Surf. Sci.*, in press, DOI: 10.1016/j.apsusc.2014.06.108.
- [32] Choi, S. K.; Kim, S.; Lim, S. K.; Park, H. Photocatalytic comparison of TiO₂ nanoparticles and electrospun TiO₂ nanofibers: Effects of mesoporosity and interparticle charge transfer. *J. Phys. Chem. C* **2010**, *114*, 16475–16480.
- [33] Zhang, Q.; Joo, J. B.; Lu, Z. D.; Dahl, M.; Oliveira, D. Q. L.; Ye, M. M.; Yin, Y. D. Self-assembly and photocatalysis of mesoporous TiO₂ nanocrystal clusters. *Nano Res.* **2011**, *4*, 103–114.
- [34] Yu, Y. X.; Xu, D. S. Single-crystalline TiO₂ nanorods: Highly active and easily recycled photocatalysts. *Appl. Catal. B-environ.* **2007**, *73*, 166–171.
- [35] Pandiaraj, S.; Aiyappa, H. B.; Banerjee, R.; Kurungot, S. Post modification of MOF derived carbon via g-C₃N₄ entrapment for an efficient metal-free oxygen reduction reaction. *Chem. Commun.* **2014**, *50*, 3363–3367.
- [36] Liu, C.; Tang, J. Y.; Chen, H. M.; Liu, B.; Yang, P. D. A fully integrated nanosystem of semiconductor nanowires for direct solar water splitting. *Nano Lett.* **2013**, *13*, 2989–2992.
- [37] Yan, S. C.; Li, Z. S.; Zou, Z. G. Photodegradation performance of g-C₃N₄ fabricated by directly heating melamine. *Langmuir* **2009**, *25*, 10397–10401.
- [38] Wu, M. C.; Sapi, A.; Avila, A.; Szabo, M.; Hiltunen, J.; Huuhtanen, M.; Toth, G.; Kukovec, . Konya, Z.; Keiski, R. et al. Enhanced photocatalytic activity of TiO₂ nanofibers and their flexible composite films: Decomposition of organic dyes and efficient H₂ generation from ethanol-water mixtures. *Nano Res.* **2011**, *4*, 360–369.
- [39] Liang, Y. Y.; Wang, H. L.; Casalongue, H. S.; Chen, Z.; Dai, H. J. TiO₂ nanocrystals grown on graphene as advanced photocatalytic hybrid materials. *Nano Res.* **2010**, *3*, 701–705.
- [40] Wang, S. P.; Li, C. J.; Wang, T. W.; Zhang, P.; Li, A.; Gong, J. L. Controllable synthesis of nanotube-type graphitic C₃N₄ and their visible-light photocatalytic and fluorescent properties. *J. Mater. Chem. A* **2014**, *2*, 2885–2890.
- [41] Gao, D. Q.; Xu, Q.; Zhang, J.; Yang, Z. L.; Si, M. S.; Yan, Z. J.; Xue, D. S. Defect-related ferromagnetism in ultrathin metal-free g-C₃N₄ nanosheets. *Nanoscale* **2014**, *6*, 2577–2581.
- [42] Dai, K.; Lu, L. H.; Liu, Q.; Zhu, G. P.; Wei, X. Q.; Bai, J.; Xuan, L. L.; Wang, H. Sonication assisted preparation of graphene oxide/graphitic-C₃N₄ nanosheet hybrid with reinforced photocurrent for photocatalyst application. *Dalton Trans.* **2014**, *43*, 6295–6299.
- [43] Liu, C.; Jing, L. Q.; He, L. M.; Luan, Y. B.; Li, C. M. Phosphate-modified graphitic C₃N₄ as efficient photocatalysts for degrading colorless pollutants by promoting O₂ adsorption. *Chem. Commun.* **2014**, *50*, 1999–2001.
- [44] Parida, K. M.; Pany, S.; Naik, B. Green synthesis of fibrous hierarchical meso-macroporous N doped TiO₂ nano-photocatalyst with enhanced photocatalytic H₂ production. *Int. J. Hydrogen. Energ.* **2013**, *38*, 3545–3553.
- [45] Sing, K. S. W.; Everett, D. H.; Haul, R. A. W.; Moscou, L.; Pierotti, R. A.; Rouquerol, J.; Siemieniewska, T. Reporting physisorption data for gas/solid systems with special reference to the determination of surface area and porosity. *Pure Appl. Chem.* **1985**, *57*, 603–619.
- [46] Zhang, J. Y.; Wang, Y. H.; Jin, J.; Zhang, J.; Lin, Z.; Huang, F.; Yu, J. G. Efficient visible-light photocatalytic hydrogen evolution and enhanced photostability of core/shell CdS/g-C₃N₄ nanowires. *ACS Appl. Mater. Inter.* **2013**, *5*, 10317–10324.
- [47] Gu, L. A.; Wang, J. Y.; Zou, Z. J.; Han, X. J. Graphitic-C₃N₄-hybridized TiO₂ nanosheets with reactive {001} facets to enhance the UV- and visible-light photocatalytic activity. *J. Hazard. Mater.* **2014**, *268*, 216–223.